Additive Manufacturing Letters 4 (2023) 100111

Contents lists available at ScienceDirect

Additive Manufacturing Letters

journal homepage: www.elsevier.com/locate/addlet

Short Communication

Inelastic finite deformation beam modeling, simulation, and validation of additively manufactured lattice structures

Oliver Weeger [a,*], Iman Valizadeh [a], Yash Mistry [b], Dhruv Bhate [b]

[a] Department of Mechanical Engineering, Additive Manufacturing Center & Centre for Computational Engineering, Technical University of Darmstadt, Dolivostr. 15, Darmstadt 64293, Hessen, Germany

[b] 3DX Research Group, Arizona State University, 6075 S. Innovation Way West, Mesa, AZ 85212, Arizona, United States

ARTICLE INFO

Keywords:
Lattice structures
Nonlinear beam model
Elasto-visco-plasticity
Laser sintering
Vat photopolymerization

ABSTRACT

Lattice-type periodic metamaterials with beam-like struts have been extensively investigated in recent years thanks to the progress in additive manufacturing technologies. However, when lattice structures are subject to large deformations, computational simulation for design and optimization remains a major challenge due to complex nonlinear and inelastic effects, such as instabilities, contacts, rate-dependence, plasticity, or damage. In this contribution, we demonstrate for the first time the efficient and accurate computational simulation of beam lattices using a finite deformation 3D beam formulation with inelastic material behavior, instability analysis, and contacts. In particular, the constitutive model captures elasto-visco-plasticity with damage/softening from the Mullins effect. Thus, the formulation can be applied to the modeling of both stiffer metallic and more flexible polymeric materials. The approach is demonstrated and experimentally validated in application to additively manufactured lattice structures made from Polyamide 12 by laser sintering and from a highly viscous polymer by vat photopolymerization. For compression tests executed until densification or with unloading and at different rates, the beam simulations are in very good agreement with experiments. These results strongly indicate that the consideration of all nonlinear and inelastic effects is crucial to accurately model the finite deformation behavior of lattice structures. It can be concluded that this can be effectively attained using inelastic beam models, which opens the perspective for simulation-based design and optimization of lattices for practical applications.

1. Introduction

Architected materials such as lattice structures and periodic metamaterials have received a tremendous amount of attention in recent years due to the mechanical and multifunctional properties that they can exhibit, as well as the possibility to effectively realize them by additive and other emerging advanced manufacturing (AM) technologies [1]. In particular, the mechanical behaviors of lattices constituted of truss- or beam-like struts are highly tailorable. By the choice of base materials and micro-architectures, properties such as the stretchability and compressibility [2,3], anisotropic, auxetic, chiral, or oligomodal behavior [4–6], resilience, damage-tolerance and failure [7–9], uncertainties, instabilities, or rate-dependence [10–14], energy absorption and dissipation [15–17], or multi-physical behaviors such as shape memory and active deformations [18,19] can be achieved.

Main drivers for the industrial adoption of lattice structures are the performance and material efficiency improvements, as well as the individualization made possible by AM. Besides material and manufacturing advancements, simulation-based design and optimization of lattices is a key ingredient. When restricted to the linear elastic range, which applies to “stiff” lattice structures or, more general, to metamaterials with minimal compliance, full-scale and multiscale simulation and optimization are well established using both analytical and numerical methods [20–24]. However, for “soft” lattice structures that can exhibit at least moderate deformations, instabilities and contacts occur along with inelastic effects such as rate-dependence, plasticity, damage, or failure, which makes computational simulation much more challenging [1,25].

So far most works that compare experimental and modeling results employ nonlinear and inelastic 3D continuum finite element methods, c.f. [2,8,9,12,14,15,19], achieving varying degrees of agreement between experiments and simulations at very high computational costs [26–29]. However, in particular for lattices with slender struts, computationally more efficient beam models would be highly desirable to facilitate extensive parameter studies, design optimization, or uncertainty quantification.

Though first steps in this direction have been made [30–34], to the best of our knowledge, the applicability of finite deformation inelastic 3D beam modeling of lattice structures has so far only been

* Corresponding author.
E-mail address: weeger@cps.tu-darmstadt.de (O. Weeger).

https://doi.org/10.1016/j.addlet.2022.100111
Received 11 October 2022; Received in revised form 21 November 2022; Accepted 27 November 2022

demonstrated and validated for metallic lattices considering plasticity and damage/fracture [35,36], as well as viscoelastic polymeric lattices [16]. Thus, the aims of this manuscript are to show that (i) inelastic material models for beams with elasto-visco-plasticity and damage can be calibrated to relatively simple experimental data, (ii) inelastic beam formulations can accurately predict the mechanical behavior of lattices subject to large deformations with instabilities and contacts, and that (iii) it is crucial to consider all relevant inelastic phenomena to obtain qualitatively meaningful simulation results.

2. Methods

2.1. Finite deformation inelastic 3D beam model

To simulate the mechanical deformation of 3D lattice structures, the struts are here modeled as geometrically exact beams, often referred to as Cosserat rods, or Timoshenko or Simo–Reissner beams [37–39]. This theory accounts for large deformations and rotational changes and includes shear effects, but is limited to small to moderate strains since the cross-sections are assumed to remain undeformed and plane, and linear constitutive models are employed. Nevertheless, it can also be extended to inelastic material behavior [40,41], which is very briefly summarized in the following.

A geometrically exact beam of length L is represented by its arc-length parameterized centerline curve $\boldsymbol{r}(s)$ and the cross-section orientation in terms of a rotation matrix field $\boldsymbol{R}(s)$. Figure 1a illustrates the initial configurations of 8 differently oriented beams that constitute a body-centered cubic (BCC) unit cell. The initial centerline curves $\mathring{\boldsymbol{r}}(s)$ are shown in gray, the two cross-section directors $\mathring{\boldsymbol{d}}_1, \mathring{\boldsymbol{d}}_2$ given by $\mathring{\boldsymbol{R}}(s) = (\mathring{\boldsymbol{d}}_1, \mathring{\boldsymbol{d}}_2, \mathring{\boldsymbol{d}}_3 = \mathring{\boldsymbol{r}}')$ as red and green arrows, and the solid cross-sections are indicated transparently. The kinematics of the beam are expressed in terms of two strain measure vectors:

$$\begin{aligned} \boldsymbol{\varepsilon}(s) &= \boldsymbol{R}^\top \boldsymbol{r}' - \mathring{\boldsymbol{R}}^\top \mathring{\boldsymbol{r}}', \\ \boldsymbol{\kappa}(s) &= \boldsymbol{k} - \mathring{\boldsymbol{k}} \quad \text{with} \quad \boldsymbol{k} = \operatorname{axl}(\boldsymbol{R}'^\top \boldsymbol{R}), \end{aligned} \tag{1}$$

which express shear strains, axial stretch, bending curvatures, and twist. The quasi-static mechanical equilibrium of the beam is then described by the balance of linear and angular momentum:

$$\begin{aligned} \boldsymbol{n}' + \boldsymbol{f} &= \boldsymbol{0} \\ \boldsymbol{m}' + \boldsymbol{r}' \times \boldsymbol{n} &= \boldsymbol{0} \quad \forall s \in (0, L). \end{aligned} \tag{2}$$

The internal forces and moments are related to the stress resultants as $\boldsymbol{n}(s) = \boldsymbol{R}(s)\boldsymbol{\sigma}(s)$, $\boldsymbol{m}(s) = \boldsymbol{R}(s)\boldsymbol{\chi}(s)$, and $\boldsymbol{f}(s) = (0, 0, -\rho g)^\top$ denotes the body force.

The material model, which is required for the closure of the nonlinear system of equilibrium equations, is expressed using a Helmholtz free energy function Ψ [39]:

$$\boldsymbol{\sigma}(s) = \frac{\partial \Psi}{\partial \boldsymbol{\varepsilon}}, \qquad \boldsymbol{\chi}(s) = \frac{\partial \Psi}{\partial \boldsymbol{\kappa}}, \tag{3}$$

which can be formulated in terms of $\boldsymbol{\varepsilon}$, $\boldsymbol{\kappa}$ and further internal variables to include inelastic behaviors [41,42]:

$$\begin{aligned} \Psi(s) = \eta \Psi^e(\boldsymbol{\varepsilon} - \boldsymbol{\varepsilon}^p, \boldsymbol{\kappa} - \boldsymbol{\kappa}^p) + \Psi^d(\eta) \\ + \sum_{i=1}^{m} \Psi_i^v(\boldsymbol{\varepsilon} - \boldsymbol{\varepsilon}_i^v, \boldsymbol{\kappa} - \boldsymbol{\kappa}_i^v) + \Psi^h(\boldsymbol{\nu}, \boldsymbol{\mu}, \mu_0). \end{aligned} \tag{4}$$

This model corresponds to a generalized Maxwell rheological model with an elasto-plastic branch with damage and m visco-elastic branches, see Fig. 1b. Furthermore, to advance the internal variables and ensure thermo-dynamic consistency, i.e., the fulfillment of the Clausius–Duhem inequality $\boldsymbol{\sigma} \cdot \dot{\boldsymbol{\varepsilon}} + \boldsymbol{\chi} \cdot \dot{\boldsymbol{\kappa}} - \dot{\Psi} \geq 0$, suitable evolution equations must be defined. For plasticity, these flow rules depend on a yield function Φ, which is directly expressed in terms of the stress resultants $\boldsymbol{\sigma}$, $\boldsymbol{\chi}$ and conjugate non-equilibrium stresses of the beam model. Further details on the model formulation, in particular the (inelastic) potentials and evolution equations, are provided in Appendix A.1.

2.2. Computational simulation of lattice structures

For the numerical solution of the inelastic 3D beam model, a mixed isogeometric collocation method is employed here [41,43]. A brief summary of the approach is provided in Appendix A.2. However, it should be noted that the numerical method itself is not critical for the results presented in this work, i.e., finite element or finite difference methods could be used alternatively. Likewise, other beam models that allow the consideration of inelastic material effects could be used, e.g., the Hughes-Liu element in LS-DYNA [16,35,36].

So far, only the mechanical and computational modeling of a single beam has been introduced. For a lattice structure, each strut is modeled as a beam and discretized as described above, see also Fig. 1c. Due to the concentration of material at the lattice nodes, a rigid coupling of the struts is assumed at the joints. Thus, forces and moments are in equilibrium at each node and positions and changes of cross-section orientation are equal for all coupled beam end points, see [43] for details. Then, the coupled nonlinear system of equations is solved in order to determine the deformed configuration of the beam assembly for given boundary conditions. Here, the lattice structures are typically clamped, i.e., positions and rotations are prescribed at certain boundaries. Simulations are performed in a displacement-controlled manner, i.e., by incrementing the prescribed displacements over several load steps, typically yielding effective strain increments of 0.25–0.5% per step.

In fact, especially for polymer structures fabricated by inkjet, SLS, or MSLA, which have a high geometric accuracy and material homo-

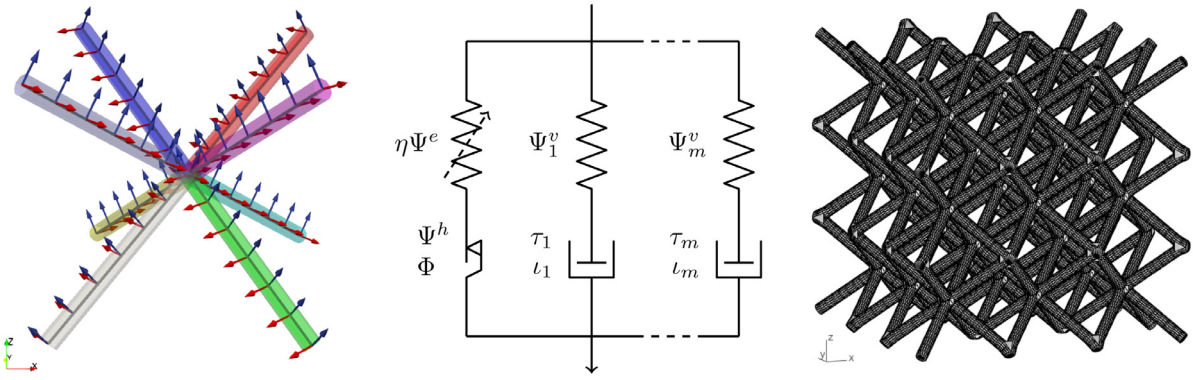

(a) Beam model of the unit cell of a BCC lattice with 8 struts

(b) Rheological model for rate-independent elasto-visco-plasticity with damage

(c) Triangulated solid representation of a BCC lattice with $3 \times 3 \times 3$ unit cells

Fig. 1. Illustration of the beam, inelastic material, and lattice structure models

geneity, the material concentration at nodes further restricts deformation and requires additional stiffening [31,44,45]. Thus, the struts are graded by increasing the diameters towards the nodes, i.e., close to the beam ends. This nodal stiffening approach with geometrically derived parameters was previously successfully applied to inkjet printed lattices [13,31].

Furthermore, beam lattices are prone to geometric instabilities such as strut buckling. To resolve these instabilities and obtain numerical convergence, post-buckling analysis methods are applied [13]. Here, a simple perturbation approach is used, in which the control points of the initial centerlines $\check{\boldsymbol{r}}_i$ are randomly perturbed [46]. The refinement of the initial NURBS functions and curves is chosen with $p_0 = 3$ and $n_0 = 4$, and the perturbations are normally distributed with 0-mean and variance $0.025d$, d being the nominal, as-designed strut diameter. Thus, the simulation results are non-deterministic and different instances of the simulations may result in different post-buckling behaviors, see e.g. Fig. 3.

Additionally, beam-to-beam contacts typically occur at large compressive displacements due to the compaction of lattice cells. To determine possible contact points, the centerlines are discretized into equally spaced candidate points and a penalty formulation is used to allow only minimal penetration when two beams intersect, see [47]. Rigid body contacts, e.g., with the plates used to apply the displacements in compression tests, are also considered.

Generally, it must be noted that the combination of finite deformations, instabilities, contacts, and inelastic material behavior make this simulation problem highly nonlinear and non-convex, i.e., the solutions non-unique. Thus, for increasing compaction with a multitude of contacts and plastic zones, convergence can be difficult to achieve and the numerical method may diverge.

2.3. Experimental methodologies

The inelastic beam modeling framework as presented above is applied to lattice structures realized by two different polymer materials and additive manufacturing processes, i.e., laser sintering (SLS) and vat photopolymerization (masked stereolithography, MSLA).

For the SLS process, an EOS FORMIGA P 110 machine is used with Polyamide 12 (PA12, nylon) as material. Uniaxial tension tests with standard specimens for material characterization according to ASTM D638-14 and compression tests of 3D printed lattices are carried out on an Instron 5985 testing machine with a 250 kN load cell.

For the MSLA process, a Prusa SL1S 3D printer and the Prusament Resin Tough Prusa Orange are used. The main printing parameters are the layer height of 0.05 mm and the cure time per layer of 3 s. Here, the material characterization experiments and lattices compression tests are performed on a MFC T500-1200 testing machine with a 5 kN load cell.

All experiments are executed at room temperature and temperature-dependence of the materials and models is not considered.

The lattice geometries are designed in Rhino 6 with the IntraLattice plug-in for Grasshopper. From this software, the centerline curves (which are here always straight lines and can be described with $p_0 = 1$, $n_0 = 2$) are exported in a NURBS format for the simulations and the solid geometries are exported as STL triangulations for 3D printing, see Fig. 1a.

3. Results and discussion

3.1. Lattice structures fabricated by laser sintering

The nonlinear simulation approach based on an inelastic 3D beam model is first demonstrated in application to lattices laser sintered from Polyamide 12.

In order to characterize the material model for PA12, uniaxial tensile tests are carried out on standard specimens at four strain rates

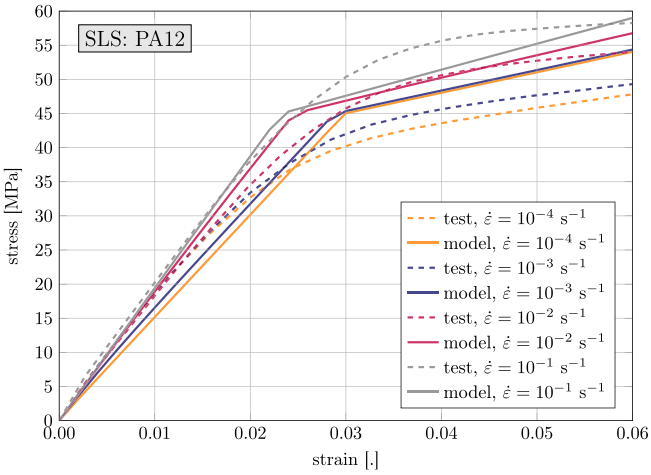

Fig. 2. Characterization of the material model for the laser sintered Polyamide 12 based on uniaxial tension tests

$\dot{\varepsilon} = 10^{-4}, 10^{-3}, 10^{-2}, 10^{-1}$ s^{-1}. For each strain rate, three tests are executed and the corresponding averaged stress–strain curves are shown in Fig. 2. Then, the parameters of the rate-independent elasto-visco-plastic constitutive model are fitted to the experimental results, see also Fig. 2, as well as Appendix A.3 for further details and Eq. (A.11) for parameter values. A reasonable agreement in terms of the rate-dependence of the visco-elastic range, the onset of yield, and the plastic hardening behavior is obtained.

Next, BCC lattices with $3 \times 3 \times 3$ unit cells of cell size $L_c = 15$ mm with circular cross-sections at two strut diameters $d = 1.2, 1.8$ mm are fabricated from PA12 by SLS, see Fig. 3. As can be seen in Fig. 3a, at the top and bottom almost rigid plates are attached so that the struts can be considered as fully clamped there. For each diameter, three specimens are subjected to compression tests up to $u = 25$ mm applied displacement (equivalent to $\varepsilon = 55.6\%$ effective compressive strain) at the deformation rate $\dot{u} = 1$ mm/s, see Fig. 3b,c. The snapshots and force–displacement curves in Fig. 3 show that the deformation behavior of the structures is generally characterized by a compression-dominated elastic initial phase, followed by buckling of the mid layer of cells that leads to elastic softening in some struts and yielding in others (see $u = 6$ mm in Fig. 3a), and then compaction that causes beam-to-beam contacts ($u = 11$ mm), which lead to a stiffer overall response ($u = 14$ mm) until also the top and bottom layers buckle ($u = 24$ mm). The experimental test results of all three specimens are qualitatively and quantitatively fairly consistent for both diameters until the second instability occurs. This can be explained by manufacturing tolerances having only a minor effect on the load at which the first instability occurs, but possibly leading to (slightly) different buckling patterns. Once the lattices compact, the contacts lead to a similar load increase, but may ultimately cause very different post-buckling patterns with consequently different plastified areas, producing a large variety of behaviors and load levels.

The simulation of the lattice structures with a total of 216 struts is also carried out three times for each diameter with different randomized perturbations of the centerline curves. The rate-independent elasto-visco-plastic material model with parameters as specified in Eq. (A.11) is employed. The resulting force–displacement curves plotted in Fig. 3b,c show a good qualitative and quantitative agreement with the experimental test results. The highly complex deformation behavior of the lattice with instabilities, plastification and contacts is well reproduced, as can also be seen by visual comparison of the snapshots in Fig. 3a. Since the applied perturbations are relatively small, the simulation curves coincide almost perfectly until the second instability occurs. Then, they exhibit also fairly different behaviors, especially for $d = 1.2$ mm, which is again very similar to the experiments.

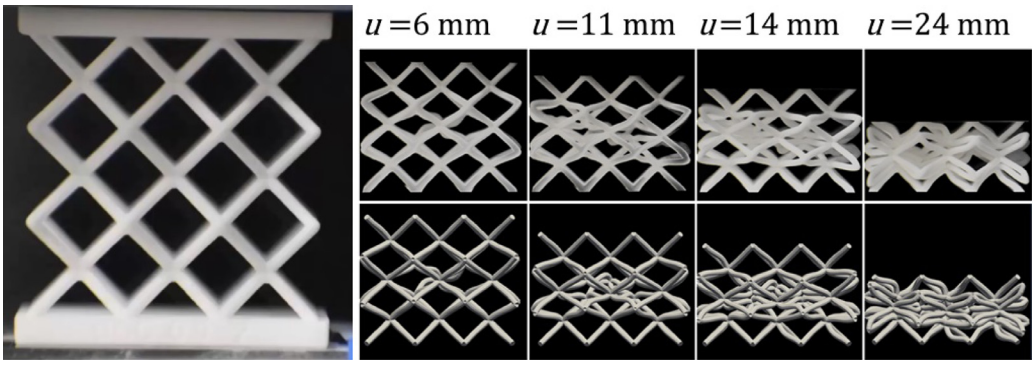

(a) Printed lattice with $d = 1.8$ mm (left) and comparison of snapshots of the deformed structure in experiment (top) and in simulation (bottom) at various applied deformations u

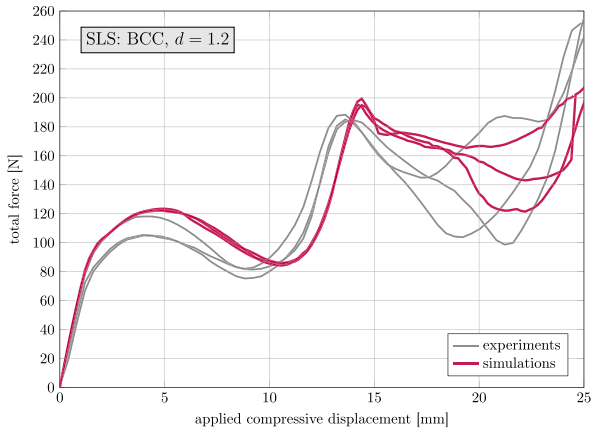

(b) Force–displacement curves for $d = 1.2$ mm

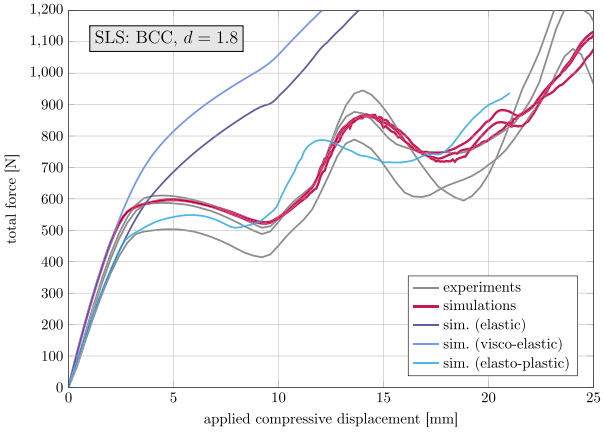

(c) Force–displacement curves for $d = 1.8$ mm

Fig. 3. Compression tests of SLS printed $3 \times 3 \times 3$ BCC lattice structures (curves of the same color indicate different instances of the same experiment or simulation)

Additionally, Fig. 3c shows curves for simulations for $d = 1.8$ mm using a purely elastic, visco-elastic, and elasto-plastic material model. It can be seen that plasticity is crucial to obtain the initial instability and softening behavior, otherwise the force response is severely overestimated. Visco-elasticity is required to capture the rate-dependence of the (initial) stiffness and relaxation behavior. Overall, this shows that modeling inelastic effects is crucial to even qualitatively predict the deformation behavior of lattice structures and that this can be accurately achieved by a inelastic beam formulation – though the aspect ratios $a_c = d/L_c$ are only moderately slender with 0.08 and 0.12.

3.2. Lattice structures fabricated by photopolymerization

Now, the inelastic beam modeling approach is applied to lattice structures manufactured by MSLA of a photopolymer with highly viscous behavior.

For the experimental characterization of the material model, cyclic uniaxial tension tests with loading up to 3%, 6% and 9% strain followed by immediate unloading at the same strain rate, as well as stress relaxation tests with loading up to 2% strain and holding of the applied deformation/strain are performed at different strain rates. The averaged stress–strain curves of 3 tests each in Fig. 4 show that this material behaves much more viscous than PA12, exhibiting strong rate-dependence and considerable stress relaxation even when loaded at the lowest rate $\dot{\varepsilon} = 4 \cdot 10^{-5}$ s^{-1}. The parameters of the now rate-dependent elasto-visco-plastic constitutive model with damage are fitted to the cyclic and relaxation tests, see also Fig. 4 and Eq. (A.12) for parameter values. The loading and relaxation behavior can be described very well by the model. Only the unloading behavior in the cyclic tension tests shows larger deviations, which may be related to the limitations of the simple plasticity model or the damage model.

BCC lattices structures with $3 \times 3 \times 3$ RUCs are fabricated by MSLA, see Fig. 5. The cell size is $L_c = 10$ mm and the strut diameters of the circular cross-sections are $d = 0.9, 1.2$ mm, i.e., the aspect ratios are $a_c = 0.09, 0.12$. As before, at the top and bottom almost rigid plates are attached to fully clamp the struts there, see Fig. 5a. The specimens are subjected to compression tests at two deformation rates $\dot{u} = 0.375, 3.75$ mm/min, which are executed in a cyclic fashion, i.e., with loading up to an applied displacement $u = 4.5$ mm, corresponding to an effective strain $\varepsilon = 15\%$, and then unloading. Additionally, for $d = 0.9$ mm cyclic tests are carried out with loading up to $u = 6.0$ mm or $\varepsilon = 20\%$. The force–displacement curves for theses experimental tests are shown in Fig. 5b,c.

The simulations of the lattices are carried out with the rate-dependent elasto-visco-plastic material model with damage with parameters as specified in Eq. (A.12), again using different randomized perturbations of the initial centerline curves. For the thicker structure with $d = 1.2$ mm, four snapshots of the deformed lattice structure (on the loading path) in experiment and simulation are shown in Fig. 5a. Visually, a good agreement of the deformation patterns can be observed. Furthermore, the also the force–displacement curves plotted in Fig. 5b are in an excellent qualitative and quantitative agreement in the elastic loading, the post-buckling and plastification, as well as the unloading phases. Importantly, the behavior at both strain rates is predicted equally well. For the thinner structure with $d = 0.9$ mm, the plots in Fig. 5c also show a good agreement of the experimental and simulation results with slightly larger deviations, which are also present in the different experimental instances. However, in order to obtain these results and not to significantly over-predict the responses for $d = 0.9$ mm, in

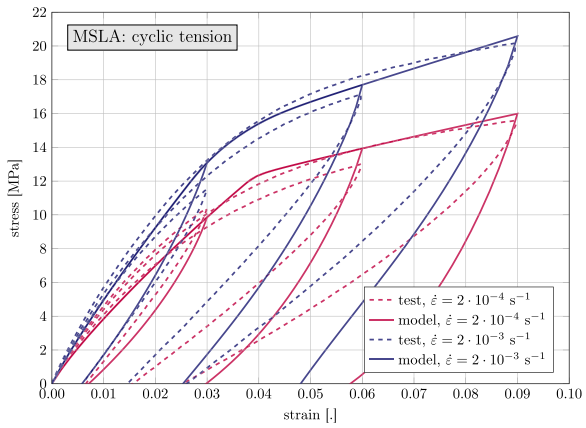

(a) Cyclic tension tests and model fits

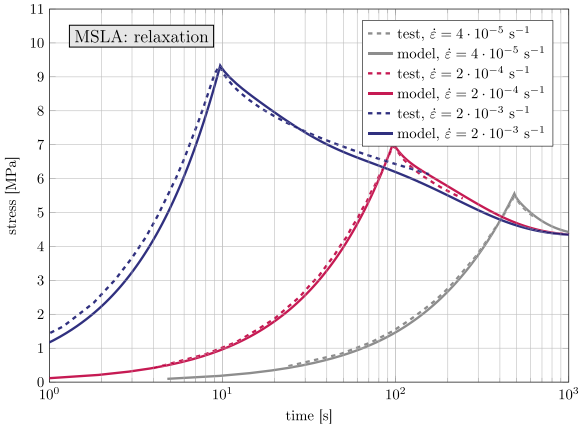

(b) Relaxation tests at 2% strain and model fits

Fig. 4. Characterization of the material model for the MSLA printed polymer

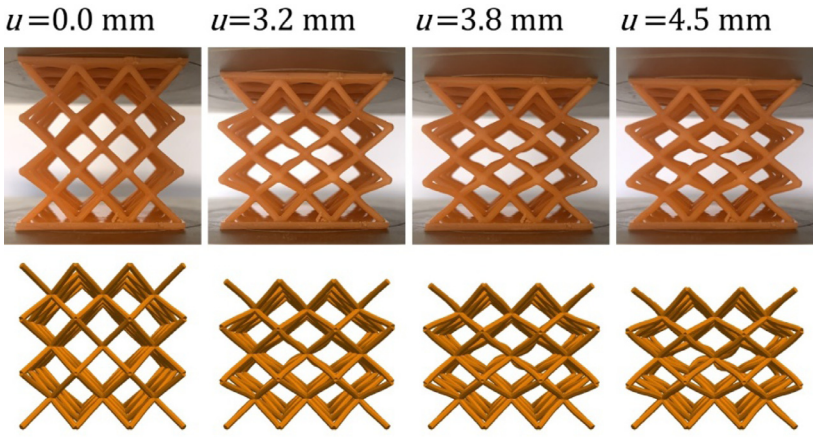

(a) Comparison of snapshots of deformed structure with $d = 1.2$ mm in experiment (top) and simulation (bottom) at various applied deformations u

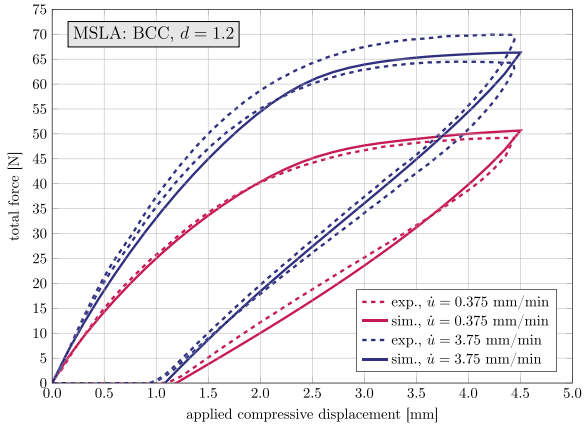

(b) Force–displacement curves for $d = 1.2$ mm

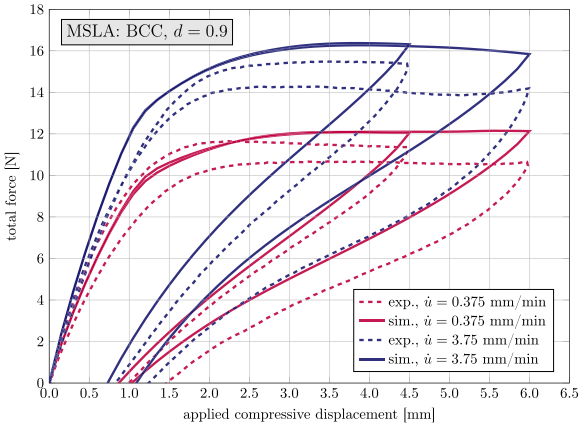

(c) Force–displacement curves for $d = 0.9$ mm

Fig. 5. Cyclic compression tests of MSLA printed $3 \times 3 \times 3$ BCC lattice structures.

the simulations the strut diameters had to be reduced to $d = 0.85$ mm and the Young's modulus to $E = 210$ MPa. These corrections can be justified by a likely decay in light intensity of the MSLA printer due to many other objects being printed in between the material characterization tests (and the structures with $d = 1.2$ mm) and these lattices with $d = 0.9$ mm, which potentially led to a reduction of the degree of cure and thus the material stiffness, see [48]. Furthermore, there could be geometric deviations in the order of the printer resolution of 0.05 mm [49], which could have a more significant impact on the mechanical behavior compared to the structures with $d = 1.2$ mm.

These observations and explanations are also confirmed by another lattice structure, consisting of $3 \times 3 \times 3$ Octahedron RUCs with $L_c = 10$ mm and $d = 0.8$ mm, see Fig. 6. The printed lattice and simulation model are shown in Fig. 6a and the force–displacement curves for cyclic compression tests up to $u = 4.5, 6.0$ mm applied deformation at different rates $\dot{u} = 0.375, 3.75$ mm/min are plotted in Fig. 6b. Again, a very good agree-

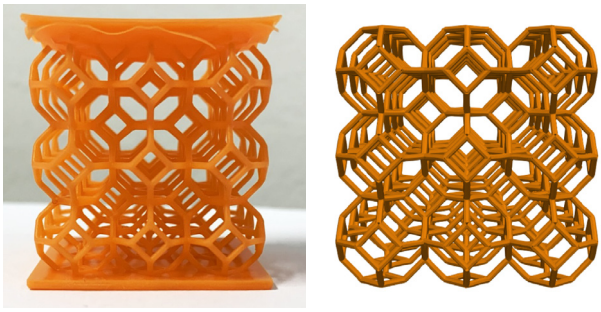

(a) Printed Octahedron lattice structure and model

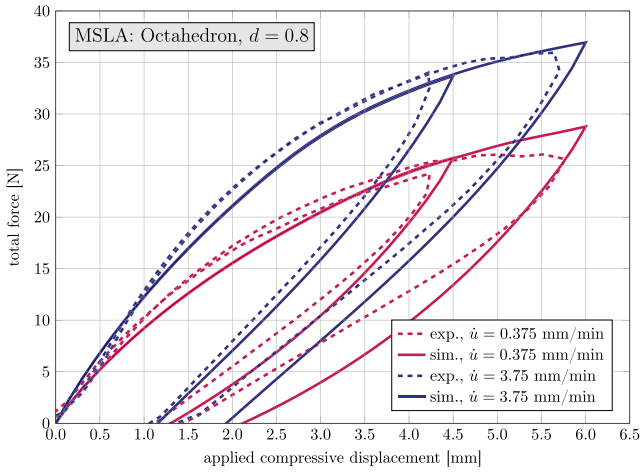

(b) Force–displacement curves

Fig. 6. Cyclic compression tests of MSLA printed $3 \times 3 \times 3$ Octahedron lattice structures

ment of the experimental and simulation results can be observed in both loading and unloading and for both rates. However, also for these Octahedron lattices, which have a small strut diameter $d = 0.8$ mm and were printed at the same time as the BCC lattices with $d = 0.9$ mm, it was necessary to set $E = 210$ MPa and $d = 0.76$ mm in the simulations.

Altogether, this application to MSLA 3D printing shows that also highly viscous, rate-dependent, and unloading behavior of lattices, in combination with instabilities, plasticity, and damage, can be accurately modeled using the inelastic beam model. The effects of manufacturing uncertainties resulting in deviations of material and geometric properties should be further investigated in future research, which is facilitated by the beam modeling approach.

4. Conclusions

In this work, the application of a 3D beam formulation, which considers elasto-visco-plastic material behavior and damage, as well as finite deformations with instabilities and contacts, to the modeling of additively manufactured beam lattice structures was presented. The inelastic material models for SLS printed PA12 and a MSLA printed photopolymer were characterized by relatively simple uniaxial tension tests at different strain rates, including cyclic loading and relaxation. Then, a qualitatively and quantitatively good agreement of experimental compression tests of additively manufactured lattice specimens with the numerical simulations of the structures using the inelastic beam model could be achieved. Furthermore, it was shown that the consideration of all relevant inelastic phenomena, instabilities, and contacts is necessary to obtain meaningful simulation results that reflect the highly nonlinear and complex deformation behavior of the loading and unloading of beam lattices.

Since the simulations using beam models are computationally more efficient than 3D continuum finite element analyses, especially when instabilities and contacts occur, these results could pave the way for a broader industrial application of lattice structures, which requires accurate and efficient simulations to shorten design cycles. Furthermore, also the design optimization of lattices subject to large deformations may become attainable [50].

Nevertheless, a limitation of this work is that the temperature-dependence of the materials and heat flow have not been considered. For instance, for PA12, temperature-dependent material models have already been investigated [51,52] and the beam model could be further extended in this direction. Furthermore, for stiffer and brittle materials such as ABS or metals, fracture should be taken into account to model highly compressed lattices. On the other hand, for soft elastomers such as TPU, the elastic nonlinearity would be more pronounced for highly stretched lattices and the beam model could be extended to nonlinear hyperelasticity.

Code and data availability

The method was implemented into a `C++` program code, which is based on the open-source isogeometric analysis library `G+SMo` [53], but not part of it. The code is available from O.W. upon reasonable request. All experimental and simulation data related to the models and figures in this manuscript is available under a CC BY 4.0 license in the public repository https://github.com/CPShub/sim-data.

Declaration of Competing Interest

The authors declare that they have no known competing financial interests or personal relationships that could have appeared to influence the work reported in this paper.

Data availability

Data will be made available on request.

Acknowledgments

O.W. acknowledges financial support of the Deutsche Forschungsgemeinschaft (DFG, German Research Foundation) – grant nos. 460684687, 492770117.

Appendix A

A1. Inelastic beam material model

As already mentioned in Section 2.1, the main ingredients of a thermo-dynamically consistent constitutive model for the 3D beam formulation are a Helmholtz free energy function Ψ, see Eq. (4), from which the stress resultants can be derived, see Eq. (3), and evolution equations for the internal variables that are required to evaluate Ψ [42].

Following [41], here the free energy is additively decomposed into the elastic strain energy potential Ψ^e, as well as the internal energy potentials for damage Ψ^d, the viscous dash-pots Ψ_i^v, and plastic hardening Ψ^h. The related additional internal variables are the scalar damage factor η for the Mullins effect, the plastic strain vectors $\boldsymbol{\varepsilon}^p, \boldsymbol{\kappa}^p$, the kinematic hardening vectors $\boldsymbol{\nu}, \boldsymbol{\mu}$, the isotropic hardening variable μ_0, and the viscous strain vectors $\boldsymbol{\varepsilon}_i^v, \boldsymbol{\kappa}_i^v$.

The potentials are typically assumed as quadratic, e.g., for homogeneous cross-sections as:

$$\begin{aligned} \Psi^e(\tilde{\boldsymbol{\varepsilon}}, \tilde{\boldsymbol{\kappa}}) &= \tfrac{1}{2}\tilde{\boldsymbol{\varepsilon}} \cdot \boldsymbol{A} \cdot \tilde{\boldsymbol{\varepsilon}} + \tfrac{1}{2}\tilde{\boldsymbol{\kappa}} \cdot \boldsymbol{C} \cdot \tilde{\boldsymbol{\kappa}}, \\ \Psi_i^v(\tilde{\boldsymbol{\varepsilon}}, \tilde{\boldsymbol{\kappa}}) &= \tfrac{1}{2}\tilde{\boldsymbol{\varepsilon}} \cdot \boldsymbol{A}_i^v \cdot \tilde{\boldsymbol{\varepsilon}} + \tfrac{1}{2}\tilde{\boldsymbol{\kappa}} \cdot \boldsymbol{C}_i^v \cdot \tilde{\boldsymbol{\kappa}}, \\ \Psi^h(\boldsymbol{\nu}, \boldsymbol{\mu}, \mu_0) &= \tfrac{1}{2}\boldsymbol{\nu} \cdot \boldsymbol{A}^h \cdot \boldsymbol{\nu} + \tfrac{1}{2}\boldsymbol{\mu} \cdot \boldsymbol{C}^h \cdot \boldsymbol{\mu} + \tfrac{1}{2}H^h \mu_0^2. \end{aligned} \tag{A.1}$$

For the elastic potential, it is $\boldsymbol{A} = \mathrm{diag}(k_1 GA, k_2 GA, EA)$ and $\boldsymbol{C} = \mathrm{diag}(EI_1, EI_2, GJ)$, with E being the Young's modulus and G the shear modulus of the material, A the area, $I_{1,2}$ the second moments of area, and J the polar moment of the cross-section. Here, only circular cross-sections with radius r and diameter $d = 2r$ are considered, for which $A = \pi r^2$, $I_1 = I_2 = \frac{\pi r^4}{12}$, $J = I_1 + I_2$, $k_1 = k_2 = \frac{5}{6}$ holds. For simplicity, the material matrices of the dissipation potentials are expressed as $\boldsymbol{A}_i^v = \zeta_i \boldsymbol{A}$, $\boldsymbol{C}_i^v = \vartheta_i \boldsymbol{C}$ with viscosity factors $\zeta_i, \vartheta_i \geq 0$, and $\boldsymbol{A}^h = \zeta_h \boldsymbol{A}$, $\boldsymbol{C}^h = \vartheta_h \boldsymbol{C}$ with kinematic hardening factors $\zeta_h, \vartheta_h \geq 0$. The isotropic hardening factor is $H^h \geq 0$.

In analogy to the Maxwell rheological model, the evolution equations for the m visco-elastic branches are expressed using the relaxation times $\tau_i, \imath_i > 0$ as:

$$\dot{\boldsymbol{\varepsilon}}_i^v = \frac{1}{\tau_i}(\boldsymbol{\varepsilon} - \boldsymbol{\varepsilon}_i^v), \qquad \dot{\boldsymbol{\kappa}}_i^v = \frac{1}{\imath_i}(\boldsymbol{\kappa} - \boldsymbol{\kappa}_i^v). \tag{A.2}$$

The elasto-plastic internal strain and hardening variables are governed by the flow rules:

$$\begin{aligned} \dot{\boldsymbol{\varepsilon}}_p &= \dot{\lambda}\frac{\partial \Phi}{\partial \boldsymbol{\sigma}}, \qquad \dot{\boldsymbol{\kappa}}_p = \dot{\lambda}\frac{\partial \Phi}{\partial \boldsymbol{\chi}}, \\ \dot{\boldsymbol{\nu}} &= \dot{\lambda}\frac{\partial \Phi}{\partial \boldsymbol{g}}, \qquad \dot{\boldsymbol{\mu}} = \dot{\lambda}\frac{\partial \Phi}{\partial \boldsymbol{h}}, \qquad \dot{\mu}_0 = \dot{\lambda}\frac{\partial \Phi}{\partial h_0}. \end{aligned} \tag{A.3}$$

Here, a yield function of the form:

$$\begin{aligned} \Phi(\boldsymbol{\sigma}, \boldsymbol{\chi}, \boldsymbol{g}, \boldsymbol{h}, h_0) = &\left(\frac{\sigma_1 + \mathrm{b}\, g_1}{\sigma_1^y}\right)^2 + \left(\frac{\sigma_2 + \mathrm{b}\, g_2}{\sigma_2^y}\right)^2 + \left(\frac{\sigma_3 + \mathrm{b}\, g_3}{\sigma_3^y}\right)^2 \\ &+ \left(\frac{\chi_1 + \mathrm{b}\, h_1}{\chi_1^y}\right)^2 + \left(\frac{\chi_2 + \mathrm{b}\, h_2}{\chi_2^y}\right)^2 + \left(\frac{\chi_3 + \mathrm{b}\, h_3}{\chi_3^y}\right)^2 \\ &- \zeta_0^y (1 + \mathrm{a} h_0), \end{aligned} \tag{A.4}$$

is used, which is formulated in terms of the stress resultants and the conjugated non-equilibrium stresses:

$$\boldsymbol{g} = -\frac{\partial \Phi}{\partial \boldsymbol{\nu}}, \qquad \boldsymbol{h} = -\frac{\partial \Phi}{\partial \boldsymbol{\mu}}, \qquad h_0 = -\frac{\partial \Phi}{\partial \mu_0}. \tag{A.5}$$

The material parameters of the yield function are the yield stress resultants σ_i^y, χ_i^y, the initial yield limit ζ_0^y, and the isotropic and kinematic hardening factors a, b. Note that the definition of the yield function in terms of stress resultants of beam models is currently still a subject to of investigation [54,55].

For rate-independent plasticity, Φ and the plastic multiplier $\dot{\lambda}$ must fulfill the Karush–Kuhn–Tucker optimality conditions:

$$\dot{\lambda} \geq 0, \qquad \dot{\lambda}\Phi = 0, \qquad \Phi \leq 0. \tag{A.6}$$

For rate-dependent (visco-) plasticity, according to the Perzyna model [42], $\dot{\lambda}$ can be directly obtained as:

$$\dot{\lambda} = \frac{1}{\eta_p} < \Phi(\boldsymbol{\sigma}, \boldsymbol{\chi}, \boldsymbol{g}, \boldsymbol{h}, h_0) >, \tag{A.7}$$

with the viscosity parameter $\eta_p > 0$ and the Macaulay brackets $< x >= \frac{1}{2}(x + |x|)$.

Using the Ogden and Roxburgh model for the Mullins effect [56,57], the damage variable is directly expressed as:

$$\begin{aligned} &\eta = \eta(\boldsymbol{\varepsilon} - \boldsymbol{\varepsilon}_p, \boldsymbol{\kappa} - \boldsymbol{\kappa}_p) = 1 - \frac{1}{r_d}\mathrm{erf}\left(\frac{1}{m_d}(\Psi^e_{\max} - \Psi^e)\right) \\ &\text{with } \Psi^e_{\max}(s,t) = \max_{\tau \leq t} \Psi^e(s,\tau), \end{aligned} \tag{A.8}$$

where $r_d, m_d > 0$ are the parameters of the model. In this way, η need not be treated as an evolving internal variable and an explicit representation of Ψ^d is not required.

A2. Isogeometric collocation method

As already mentioned in Section 2.2, an isogeometric collocation method is employed here for the discretization of the inelastic beam model. This particular approach was introduced in [43] and already successfully applied for elastic large deformation design and simulation of beam lattices [31].

The main concept of isogeometric analysis is to employ spline representations for the parameterization of geometry and the discretization of solution fields [58]. For the beam model, the initial and deformed centerline curves and orientation matrix fields, which are here parameterized by unit quaternions, $\boldsymbol{R}(s) = \boldsymbol{R}(\boldsymbol{q}(s))$ with $\boldsymbol{q} \in \mathbb{R}^4$, $\|\boldsymbol{q}\| = 1$, are expressed as NURBS curves:

$$\begin{aligned} \mathring{\boldsymbol{r}}(s) &= \sum_{i=1}^{n_0} \mathring{N}_i(s)\, \mathring{\boldsymbol{r}}_i, \quad \boldsymbol{r} \approx \boldsymbol{r}_h(s) = \sum_{i=1}^{n} N_i(s)\, \boldsymbol{r}_i, \\ \mathring{\boldsymbol{q}}(s) &= \sum_{i=1}^{n_0} \mathring{N}_i(s)\, \mathring{\boldsymbol{q}}_i, \quad \boldsymbol{q} \approx \boldsymbol{q}_h(s) = \sum_{i=1}^{n} N_i(s)\, \boldsymbol{q}_i, \end{aligned} \tag{A.9}$$

where $\mathring{N}_i$ are the n_0 NURBS shape functions of degree p_0 and $\mathring{\boldsymbol{r}}_i$, $\mathring{\boldsymbol{q}}_i$ the control points that describe the initial configuration, while N_i are n NURBS of degree p and $\boldsymbol{r}_i$, $\boldsymbol{q}_i$ the (to be determined) control points of the deformed configuration. Here, $p = 6$, $n = 12$ are chosen to ensure a sufficient accuracy of the solution.

The idea of isogeometric collocation [59] is to substitute the discretization of Eq. (A.9) into the strong form of the balance Eq. (2) and evaluate it at n discrete points, the so-called collocation points s_i:

$$\begin{aligned} \boldsymbol{n}'(s_i) + \boldsymbol{f}(s_i) &= \boldsymbol{0}, \\ \boldsymbol{m}'(s_i) + \boldsymbol{r}'(s_i) \times \boldsymbol{n}(s_i) &= \boldsymbol{0}, \\ \|\boldsymbol{q}(s_i)\|^2 - 1 &= 0. \end{aligned} \tag{A.10}$$

This results in a nonlinear system of $7n$ equations that determines the n control points $\boldsymbol{r}_i$, $\boldsymbol{q}_i$ of the deformed configuration. To solve this nonlinear system, a Newton–Raphson method is used, which requires the gradients of Eq. (A.10). Furthermore, at each collocation point, the time-integration of the evolution equations of the visco-plastic internal variables Eqs. (A.2) and (A.3) is required, for which an implicit Euler method is used here [41].

Here, in fact a mixed method is used, which means that the stress resultants are separately discretized as $\boldsymbol{\sigma}_h \approx \boldsymbol{\sigma}$, $\boldsymbol{\chi}_h \approx \boldsymbol{\chi}$, which provides the advantages of higher accuracy, alleviation of locking phenomena, faster evaluation, and easier implementation, especially with the inelastic material models [41].

A3. Material parameters

As discussed in Section 3, the material parameters of the constitutive models are all obtained by fitting to characterization experiments, in which only (one-dimensional) uniaxial tension states are considered, see Figs. 2 and 4. In fact, in this way only the relation of σ_3 with ε_3 can be (accurately) characterized and the shear and bending behaviors are assumed to be consistent with the tensile behavior. Of course, a much more elaborate material characterization could be carried out, but as the results here show, this simplification already provides good qualitative and quantitative predictions of the effective lattice behavior.

In particular, the following parameters are identified for the laser sinetered PA12:

$$\begin{aligned} &E = 1500\ \mathrm{MPa}, \quad \nu = 0.45, \quad \rho = 930\ \mathrm{kg/m^3}, \\ &m = 1, \quad \zeta_1 = \vartheta_1 = 0.3, \quad \tau_1 = \imath_1 = 4.0, \\ &\sigma_i^y = 0.033 \cdot EA, \quad \chi_i^y = 0.05 \cdot EIr, \\ &\zeta_h = \vartheta_h = 0.25, \quad b = 1, \quad a = 0, \end{aligned} \tag{A.11}$$

and the MSLA printed though polymer:

$$\begin{aligned} &E = 220\ \mathrm{MPa}, \quad \nu = 0.45, \quad \rho = 1100\ \mathrm{kg/m^3}, \\ &m = 3, \quad \zeta_1 = \vartheta_1 = 0.5, \quad \tau_1 = \imath_1 = 1.2, \\ &\qquad \zeta_2 = \vartheta_2 = 0.6, \quad \tau_2 = \imath_2 = 14, \\ &\qquad \zeta_3 = \vartheta_3 = 0.65, \quad \tau_3 = \imath_3 = 220, \end{aligned} \tag{A.12}$$

$$\sigma_i^y = 0.055 \cdot EA, \quad \chi_i^y = 0.11 \cdot EIr,$$
$$\zeta_h = \vartheta_h = 0.4, \quad b = 1, \quad a = 0, \quad \eta_P = 50/A,$$
$$r_d = 0.3, \quad m_d = 0.005 \cdot EA.$$

Note that the Poisson's ratios are assumed as near incompressible with $\nu = 0.45$, but in the beam model the value is not critical, as it is only required to calculate the shear modulus $G = E/(2+2\nu)$. Furthermore, the densities are also just estimated from literature references. They are only used to computed the values of the body load in Eq. (2), which has a minor effect on the overall force response since the structures are sufficiently stiff.

Supplementary material

Supplementary material associated with this article can be found, in the online version, at 10.1016/j.addlet.2022.100111.

References

[1] J.R. Greer, V.S. Deshpande, Three-dimensional architected materials and structures: design, fabrication, and mechanical behavior, MRS Bull. 44 (10) (2019) 750–757, doi:10.1557/mrs.2019.232.

[2] Y. Jiang, Q. Wang, Highly-stretchable 3D-architected mechanical metamaterials, Sci. Rep. 6 (1) (2016), doi:10.1038/srep34147.

[3] Y. Zhang, K. Yu, K. Lee, K. Li, H. Du, Q. Wang, Mechanics of stretchy elastomer lattices, J. Mech. Phys. Solids (2022) 104782, doi:10.1016/j.jmps.2022.104782.

[4] S. Babaee, J. Shim, J.C. Weaver, E.R. Chen, N. Patel, K. Bertoldi, 3D soft metamaterials with negative Poisson's ratio, Adv. Mater. 25 (36) (2013) 5044–5049.

[5] M. Kadic, G.W. Milton, M. van Hecke, M. Wegener, 3D metamaterials, Nat. Rev. Phys. 1 (3) (2019) 198–210, doi:10.1038/s42254-018-0018-y.

[6] A. Bossart, D.M.J. Dykstra, J. van der Laan, C. Coulais, Oligomodal metamaterials with multifunctional mechanics, Proc. Natl. Acad. Sci. 118 (21) (2021), doi:10.1073/pnas.2018610118. e2018610118

[7] L.R. Meza, A.J. Zelhofer, N. Clarke, A.J. Mateos, D.M. Kochmann, J.R. Greer, Resilient 3D hierarchical architected metamaterials, Proc. Natl. Acad. Sci. 112 (37) (2015) 11502–11507, doi:10.1073/pnas.1509120112.

[8] L. Liu, P. Kamm, F. Garca-Moreno, J. Banhart, D. Pasini, Elastic and failure response of imperfect three-dimensional metallic lattices: the role of geometric defects induced by selective laser melting, J. Mech. Phys. Solids 107 (2017) 160–184, doi:10.1016/j.jmps.2017.07.003.

[9] M.-S. Pham, C. Liu, I. Todd, J. Lertthanasarn, Damage-tolerant architected materials inspired by crystal microstructure, Nature 565 (7739) (2019) 305, doi:10.1038/s41586-018-0850-3.

[10] D.M.J. Dykstra, J. Busink, B. Ennis, C. Coulais, Viscoelastic snapping metamaterials, J. Appl. Mech. 86 (11) (2019), doi:10.1115/1.4044036.

[11] S. Janbaz, F.S.L. Bobbert, M.J. Mirzaali, A.A. Zadpoor, Ultra-programmable buckling-driven soft cellular mechanisms, Mater. Horizons 6 (2019) 1138.

[12] S. Janbaz, K. Narooei, T.v. Manen, A.A. Zadpoor, Strain rate dependent mechanical metamaterials, Sci. Adv. 6 (25) (2020) eaba0616, doi:10.1126/sciadv.aba0616.

[13] M. Jamshidian, N. Boddeti, D.W. Rosen, O. Weeger, Multiscale modelling of soft lattice metamaterials: micromechanical nonlinear buckling analysis, experimental verification, and macroscale constitutive behaviour, Int. J. Mech. Sci. 188 (2020) 105956, doi:10.1016/j.ijmecsci.2020.105956.

[14] M. Gavazzoni, S. Foletti, D. Pasini, Cyclic response of 3D printed metamaterials with soft cellular architecture: the interplay between as-built defects, material and geometric non-linearity, J. Mech. Phys. Solids 158 (2022) 104688, doi:10.1016/j.jmps.2021.104688.

[15] H. Rahman, E. Yarali, A. Zolfagharian, A. Serjouei, M. Bodaghi, Energy absorption and mechanical performance of functionally graded soft-hard lattice structures, Materials 14 (6) (2021) 1366, doi:10.3390/ma14061366.

[16] S.M. Montgomery, H. Hilborn, C.M. Hamel, X. Kuang, K.N. Long, H.J. Qi, The 3D printing and modeling of functionally graded Kelvin foams for controlling crushing performance, Extreme Mech. Lett. (2021) 101323, doi:10.1016/j.eml.2021.101323.

[17] D. Yavas, Q. Liu, Z. Zhang, D. Wu, Design and fabrication of architected multimaterial lattices with tunable stiffness, strength, and energy absorption, Mater. Des. 217 (2022) 110613, doi:10.1016/j.matdes.2022.110613.

[18] Z. Ding, O. Weeger, H.J. Qi, M.L. Dunn, 4D rods: 3D structures via programmable 1D composite rods, Mater. Des. 137 (2018) 256–265, doi:10.1016/j.matdes.2017.10.004.

[19] A. Pirhaji, E. Jebellat, N. Roudbarian, K. Mohammadi, M.R. Movahhedy, M. Asle Zaeem, Large deformation of shape-memory polymer-based lattice metamaterials, Int. J. Mech. Sci. 232 (2022) 107593, doi:10.1016/j.ijmecsci.2022.107593.

[20] L.J. Gibson, M.F. Ashby, Cellular Solids - Structure and Properties, Cambridge University Press, 1997.

[21] N. Huber, Connections between topology and macroscopic mechanical properties of three-dimensional open-pore materials, Front. Mater. 5 (2018), doi:10.3389/fmats.2018.00069.

[22] J. Souza, A. Gromann, C. Mittelstedt, Micromechanical analysis of the effective properties of lattice structures in additive manufacturing, Addit. Manuf. 23 (2018) 53–69, doi:10.1016/j.addma.2018.07.007.

[23] F. Veloso, J. Gomes-Fonseca, P. Morais, J. Correia-Pinto, A.C. Pinho, J.L. Vilaa, Overview of methods and software for the design of functionally graded lattice structures, Adv. Eng. Mater. (2022) 2200483, doi:10.1002/adem.202200483.

[24] B. Telgen, O. Sigmund, D. Kochmann, Topology optimization of graded truss lattices based on on-the-fly homogenization, J. Appl. Mech. (2022) 1–40, doi:10.1115/1.4054186.

[25] D.M. Kochmann, J.B. Hopkins, L. Valdevit, Multiscale modeling and optimization of the mechanics of hierarchical metamaterials, MRS Bull. 44 (10) (2019) 773–781, doi:10.1557/mrs.2019.228.

[26] M. Bodaghi, A.R. Damanpack, G.F. Hu, W.H. Liao, Large deformations of soft metamaterials fabricated by 3D printing, Mater. Des. 131 (2017) 81–91, doi:10.1016/j.matdes.2017.06.002.

[27] B.B. Babamiri, B. Barnes, A. Soltani-Tehrani, N. Shamsaei, K. Hazeli, Designing additively manufactured lattice structures based on deformation mechanisms, Addit. Manuf. 46 (2021) 102143, doi:10.1016/j.addma.2021.102143.

[28] D.A. Porter, M.A. Di Prima, Y. Badhe, A.R. Parikh, Nylon lattice design parameter effects on additively manufactured structural performance, J. Mech. Behav. Biomed.Mater. 125 (2022) 104869, doi:10.1016/j.jmbbm.2021.104869.

[29] S. Drcker, J.K. Ldeker, M. Blecken, A. Kurt, K. Betz, B. Kriegesmann, B. Fiedler, Probabilistic analysis of additively manufactured polymer lattice structures, Mater. Des. 213 (2022) 110300, doi:10.1016/j.matdes.2021.110300.

[30] A. Desmoulins, D.M. Kochmann, Local and nonlocal continuum modeling of inelastic periodic networks applied to stretching-dominated trusses, Comput. Methods Appl. Mech.Eng. 313 (2017) 85–105, doi:10.1016/j.cma.2016.09.027.

[31] O. Weeger, N. Boddeti, S.-K. Yeung, S. Kaijima, M. Dunn, Digital design and nonlinear simulation for additive manufacturing of soft lattice structures, Addit. Manuf. 25 (2019) 39–49, doi:10.1016/j.addma.2018.11.003.

[32] C. Lestringant, B. Audoly, D.M. Kochmann, A discrete, geometrically exact method for simulating nonlinear, elastic and inelastic beams, Comput. Methods Appl. Mech.Eng. 361 (2020) 112741, doi:10.1016/j.cma.2019.112741.

[33] R.N. Glaesener, J.-H. Bastek, F. Gonon, V. Kannan, B. Telgen, B. Spttling, S. Steiner, D.M. Kochmann, Viscoelastic truss metamaterials as time-dependent generalized continua, J. Mech. Phys. Solids (2021) 104569, doi:10.1016/j.jmps.2021.104569.

[34] C. Perez-Garcia, J. Aranda-Ruiz, R. Zaera, D. Garcia-Gonzalez, Beam formulation and FE framework for architected structures under finite deformations, Eur. J. Mech. A/Solids 96 (2022) 104706, doi:10.1016/j.euromechsol.2022.104706.

[35] N. Novak, M. Vesenjak, L. Krstulovi-Opara, Z. Ren, Mechanical characterisation of auxetic cellular structures built from inverted tetrapods, Compos. Struct. 196 (2018) 96–107, doi:10.1016/j.compstruct.2018.05.024.

[36] N. Novak, M. Vesenjak, S. Tanaka, K. Hokamoto, Z. Ren, Compressive behaviour of chiral auxetic cellular structures at different strain rates, Int. J. Impact Eng. 141 (2020) 103566, doi:10.1016/j.ijimpeng.2020.103566.

[37] S. Antman, Nonlinear Problems of Elasticity, Applied Mathematical Sciences, Vol. 107, Springer, New York, 2005.

[38] J. Simo, A finite strain beam formulation. The three-dimensional dynamic problem. Part I, Comput. Methods Appl. Mech.Eng. 49 (1) (1985) 55–70, doi:10.1016/0045-7825(85)90050-7.

[39] H. Lang, J. Linn, M. Arnold, Multi-body dynamics simulation of geometrically exact cosserat rods, Multibody Syst. Dyn. 25 (3) (2011) 285–312, doi:10.1007/s11044-010-9223-x.

[40] Smriti, A. Kumar, A. Großmann, P. Steinmann, A thermoelastoplastic theory for special Cosserat rods, Math. Mech. Solids 24 (3) (2019) 686–700, doi:10.1177/1081286517754132.

[41] O. Weeger, D. Schillinger, R. Mller, Mixed isogeometric collocation for geometrically exact 3D beams with elasto-visco-plastic material behavior and softening effects, Comput. Methods Appl. Mech.Eng. 399 (2022) 115456, doi:10.1016/j.cma.2022.115456.

[42] J.C. Simo, T.J.R. Hughes, Computational Inelasticity, Springer, New York, 1998, doi:10.1007/b98904.

[43] O. Weeger, S.-K. Yeung, M. Dunn, Isogeometric collocation methods for Cosserat rods and rod structures, Comput. Methods Appl. Mech.Eng. 316 (2017) 100–122, doi:10.1016/j.cma.2016.05.009.

[44] Y. Takahashi, D. Okumura, N. Ohno, Yield and buckling behavior of Kelvin open-cell foams subjected to uniaxial compression, Int. J. Mech. Sci. 52 (2) (2010) 377–385, doi:10.1016/j.ijmecsci.2009.10.009.

[45] G. Meyer, H. Wang, C. Mittelstedt, Influence of geometrical notches and form optimization on the mechanical properties of additively manufactured lattice structures, Mater. Des. 222 (2022) 111082, doi:10.1016/j.matdes.2022.111082.

[46] T. Grtner, M. Fernndez, O. Weeger, Nonlinear multiscale simulation of elastic beam lattices with anisotropic homogenized constitutive models based on artificial neural networks, Comput. Mech. 68 (5) (2021) 1111–1130, doi:10.1007/s00466-021-02061-x.

[47] O. Weeger, B. Narayanan, M.L. Dunn, Isogeometric collocation for nonlinear dynamic analysis of Cosserat rods with frictional contact, Nonlinear Dyn. 91 (2) (2017) 1213–1227, doi:10.1007/s11071-017-3940-0.

[48] I. Valizadeh, A. Al Aboud, E. Drsam, O. Weeger, Tailoring of functionally graded hyperelastic materials via grayscale mask stereolithography 3D printing, Addit. Manuf. (2021), doi:10.1016/j.addma.2021.102108.

[49] G.I. Peterson, J.J. Schwartz, D. Zhang, B.M. Weiss, M.A. Ganter, D.W. Storti, A.J. Boydston, Production of materials with spatially-controlled cross-link density via vat photopolymerization, ACS Appl. Mater. Interfaces 8 (42) (2016) 29037–29043, doi:10.1021/acsami.6b09768.

[50] O. Weeger, Isogeometric sizing and shape optimization of 3D beams and lattice structures at large deformations, Struct. Multidiscip. Optim. 65 (2) (2022) 43, doi:10.1007/s00158-021-03131-7.

[51] J. Schneider, S. Kumar, Multiscale characterization and constitutive parameters identification of polyamide (PA12) processed via selective laser sintering, Polym. Test. 86 (2020) 106357, doi:10.1016/j.polymertesting.2020.106357.
[52] F. Shen, W. Zhu, K. Zhou, L.-L. Ke, Modeling the temperature, crystallization, and residual stress for selective laser sintering of polymeric powder, Acta Mech. 232 (9) (2021) 3635–3653, doi:10.1007/s00707-021-03020-6.
[53] B. Jüttler, U. Langer, A. Mantzaflaris, S. Moore, W. Zulehner, Geometry + simulation modules: implementing isogeometric analysis, PAMM 14 (1) (2014) 961–962, doi:10.1002/pamm.201410461.
[54] L. Herrnbck, A. Kumar, P. Steinmann, Geometrically exact elastoplastic rods: determination of yield surface in terms of stress resultants, Comput. Mech. 67 (3) (2021) 723–742, doi:10.1007/s00466-020-01957-4.
[55] L. Herrnbck, A. Kumar, P. Steinmann, Two-scale off-and online approaches to geometrically exact elastoplastic rods, Comput. Mech. (2022), doi:10.1007/s00466-022-02204-8.
[56] R.W. Ogden, D.G. Roxburgh, A pseudo elastic model for the Mullins effect in filled rubber, Proc. R. Soc. London Ser.A Math. Phys. Eng. Sci. 455 (1988) (1999) 2861–2877, doi:10.1098/rspa.1999.0431.
[57] C. Naumann, J. Ihlemann, On the thermodynamics of pseudo-elastic material models which reproduce the Mullins effect, Int. J. Solids Struct. 69-70 (2015) 360–369, doi:10.1016/j.ijsolstr.2015.05.014.
[58] T. Hughes, J. Cottrell, Y. Bazilevs, Isogeometric analysis: CAD, finite elements, NURBS, exact geometry and mesh refinement, Comput. Methods Appl. Mech. Eng. 194 (39-41) (2005).
[59] F. Auricchio, L. Beirão da Veiga, T. Hughes, A. Reali, G. Sangalli, Isogeometric collocation methods, Math. Models Methods Appl.Sci. 20 (11) (2010) 2075–2107.